

# Characterization of a Distorted Transonic Compressor Flow using Dual-Luminophore Pressure-Sensitive Paint

Martin Bitter<sup>1\*</sup>, Fabian Wartzek<sup>2</sup>, Simon Übelacker<sup>1</sup>,  
Heinz-Peter Schiffer<sup>2</sup>, Christian J. Kähler<sup>1</sup>

<sup>1</sup>Institute of Fluid Mechanics and Aerodynamics, Bundeswehr University Munich, 85577 Neubiberg, GERMANY

<sup>2</sup>Institute of Gas Turbines and Aerospace Propulsion, Technical University of Darmstadt, 64287 Darmstadt, GERMANY

\*corresponding author: martin.bitter@unibw.de

---

**Abstract** The effect of generic free stream disturbances on the stall characteristics of a transonic compressor investigated in a collaborating research unit. Experimental campaigns were performed in the Darmstadt Transonic Compressor rig at 20.000 rpm using steady and unsteady wall pressure probes as well as steady pressure-sensitive paint. A transonic compressor was led to suffer from unsteady inlet disturbances produced by a wedge-shaped distortion generator, upstream of the rotor. The experiments were carried out for various radial distortion generator positions as well as mass flow rates ranging from peak efficiency down to the near-stall regime (16.1–13.9 kg/s). Data from the pressure-sensitive paint measurements is compared to the steady surface pressure tap data with respect to accuracy and the benefit of raised spatial resolution. It was possible to resolve the sharo wall pressure gradient upstream and across the rotor disc by means of pressure-sensitive paint. These results are essential for the validation of numerical flow simulations as well as for the design of nacelles and fans.

**Keywords:** pressure-sensitive paint, compressor flow, flow distortion

---

## 1 Introduction

In times of increasing air traffic, the aviation community is striving towards steeper climb angles in order to tighten the aircraft envelope and to reduce the impact of noise on the ground, see [12]. Nevertheless, safety margins have to be met for the operation of the aircraft and its engines. At the low speed limit of the flight envelope, nacelle stall can occur. This phenomenon is highly unsteady and leads to total pressure losses in the engine inlet. The main intake's purpose is to provide homogeneous inflow conditions to the compressor and to avoid nacelle stall at high angles of attack, gusts or crosswind. The impact of a relatively small generic gust on the inner aerodynamics of a flow-through nacelle with a comparable boundary layer development as that of a powered jet engine at high mass flow rates were investigated in [13]. Because it is a design criteria and an important item for the certification, the jet engine's behavior on such disturbances is investigated in a research unit, see [10, 11].

In compressor test rigs several kinds of distortions were tested in the past. Delta wings have simulated a sucked-in ground vortex, while screens and beams induced total pressure losses due to separations at the inlet. The authors in [6] described the effect of a distortion generator simulating unsteady vortices in an inlet flow.

Experimental investigations were recently performed in the Darmstadt Transonic Compressor test facility. Since the compressor was known to be sensitive to tip distortions from [6], a beveled beam distortion generator was installed upstream of the rotor disc for the generation of unsteady inlet disturbances. The experimental campaign delivered steady and unsteady surface pressure from individual pressure taps and pressure transducers, see [17]. The pressure-sensitive paint measurement technique (PSP) was applied in a separate experimental campaign, compare with [7]. This technique allows the simultaneous measurement of static surface pressures with very high spatial resolution. The intention was to answer two key aspects: *a) How good is the performance of PSP to quantify the impact of the distortion generator on the flow topology upstream and across the compressor stage?* and *b) How is the PSP measurement accuracy affected by high surface temperatures?*

The PSP measurement technique was already applied in a number of turbomachinery applications even at high static surface temperature, e.g. [9] or [4], or for film-cooling investigations, see [16]. The undisturbed blade pressure on the rotor of the Darmstadt Transonic Compressor was already investigated by means of PSP, compare [2]. In the present work, the disturbed wall pressure distribution is measured optically and compared to probe data from [17] with respect to the key aspects.

## 2 Pressure-Sensitive Paint

The pressure-sensitive paint technique (PSP) is a luminescence application developed for the optical and contact-less measurement of surface pressure distributions in transonic flows. The technique is widely applied at large aeronautic research institutions like DLR, JAXA, ONERA or NASA (German, Japanese, French or American aerospace research institutions). It is widely applied for steady pressure measurements but also covers pressure fluctuations up to frequencies of 100 kHz, see [3].

The measuring principle is based on the detection of luminescence intensity which is emitted by photo-optically excited  $O_2$ -sensitive luminophores, typically metallo-porphyrine, pyrene or ruthenium complexes. Since their excited state is metastable, these luminophores either tend to transfer their excitation energy to oxygen molecules in their vicinity (oxygen quenching – a non-radiative relaxation) or relapse back to their ground state by releasing the extra energy as luminescence intensity if no quenching partner is available within a certain fluorescence lifetime (radiative relaxation). The  $O_2$ -concentration is directly proportional to the oxygen partial pressure, hence also to static fluid pressure, according to Henry's law. Incorporated into a binder polymer and a solvent, the solution can be applied to most of the common materials using different application techniques (eg. spraying, printing, dipping). Typically, the luminophores remain physically and photo-chemically stable for a certain time period (from hours to days).

The internal conversion of excitation energy into thermal energy is another highly likely quenching property of nearly all  $O_2$ -sensitive luminophores (known as thermal quenching). This undesired property for pressure measurements can severely decrease the measurement accuracy if the PSP surface is exposed to strong surface temperatures whose actual values are unknown. The error can reach up to several percent per Kelvin with respect to the applied luminophore. Contrary to  $O_2$ -sensitive luminophores, there are several  $T$ -sensitive luminophores (e.g. europium or perylene complexes) which can exhibit no or very small pressure dependency. These luminophores, which must be optically separated from the pressure-sensitive luminophores by a separate wavelength band, can be incorporated into the paint solution and thus can be used as optical thermometers to compensate for the temperature effect, see [8]. These dual-luminophore or two-component paints are commercially available nowadays. The luminophore's quenching ability can be formulated by the Stern-Volmer relation (1):

$$I_0/I = 1 + c_q(T) \cdot p_{O_2} \quad (1)$$

where  $I_0$  is the luminescence intensity at vacuum conditions,  $I$  the luminescence intensity at the measurement point,  $c_q(T)$  the temperature dependent quenching constant and  $p_{O_2}$  the oxygen partial pressure. The Stern-Volmer relation is reformulated for PSP applications to relation (2):

$$\left(\frac{I_{ref}}{I}\right)(T, p) = A(T) + B(T) \left(\frac{p}{p_{ref}}\right) + C(T) \left(\frac{p}{p_{ref}}\right)^2 \quad (2)$$

for the estimation of unknown static pressures  $p$ . Here,  $I_{ref}$  is the pressure and temperature dependent intensity at known reference conditions (denoted as 'wind-off' condition),  $I$  is the intensity at the unknown pressure (denoted as 'wind-on' condition) and  $A(T)$ ,  $B(T)$  and  $C(T)$  are calibration coefficients. Figure 1 shows the calibration of the dual-luminophore PSP applied on a Plexiglas (PMMA) sample as it was used for the experiments presented here. This paint has a pressure sensitivity of 70 %/100 kPa and exhibits a very small temperature dependence of 0.07 %/K, [5].

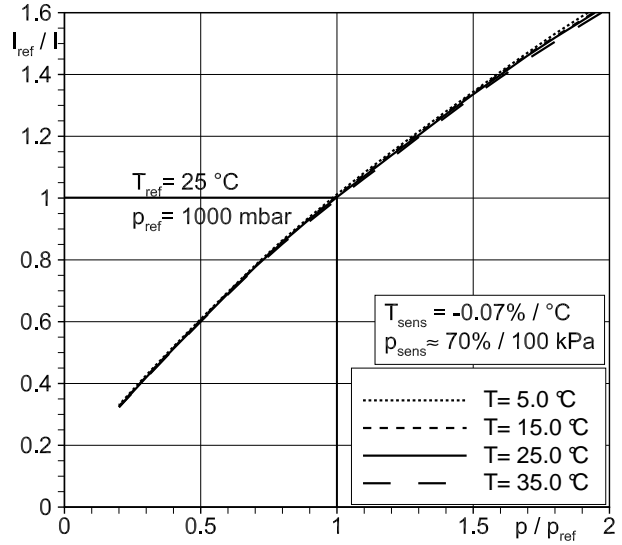


Fig. 1 Calibration plot of a dual-luminophore pressure-sensitive paint applied on a PMMA sample

### 3 Darmstadt Transonic Compressor - DTC

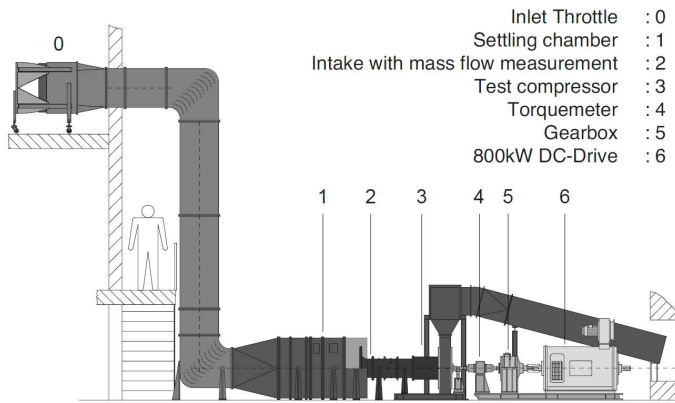


Fig. 2 Components of the Darmstadt Transonic Compressor (DTC) test rig

The experiments were carried out in the Darmstadt Transonic Compressor (DTC) facility shown in Figure 2 which was designed to characterize the performance of turbine or compressor stages. The rotor stage is driven by a 800 kW DC motor. Air is sucked-in from ambience, filtered and homogenized in the settling chamber using honey-combs. Downstream of the settling chamber, the intake massflow and total pressure values were measured in front of the compressor stage which has a diameter of 380 mm. Downstream of the stage, the air passes the outlet throttle and is guided back to ambience. A torque meter measures flow rate and torque as input for efficiency calculations. The design mass flow rate of this facility is 16 kg/s at 20.000 rpm. The mass flow is controlled by the outlet throttle. Further relevant key parameter of the DTC are given in Table 1. The characteristics of the compressor stage at  $N_{65\%}$  (13.000 rpm, *left*) and  $N_{100\%}$  (20.000 rpm, *right*) are shown in Figure 3. The rotor efficiency  $\eta_{is}$  is plotted in gray values, whereas the total pressure ratio  $\pi_t$  across the rotor stage is plotted in black. More details on the rotor stage can be found in [15].

#### 3.1 Inlet Distortion Generator

The DTC was equipped with an inlet distortion generator (DG) over one third of its circumference ( $120^\circ$ ). The intention of this device is the production of a severe local unsteady flow disturbance upstream of the rotor stage to study its effect on the efficiency and stall behavior of the rotor stage, which is known to be tip-critical, compare [6]. Figure 4 gives an impression of the flow topology downstream of the distortion generator. Here, the lateral surface of the inlet duct was unwrapped and displayed versus its arc angle  $\varphi$  while the flow approaches from the top. The wedge-shaped distortion generator with a ramp angle of  $30^\circ$  was positioned about 85 mm (twice the axial chord lengths) prior to the tip leading edge plane of the rotor and could be traversed over  $360^\circ$  in both directions. Its axial extent was 30 mm  $\equiv 20\%$  of the compressor blade's span. Downstream of the DG, a distinct separation region develops with two strong corner vortices at both ends of the DG and a low pressure region in the center. The forming of this region is slightly asymmetric due to the superposition with the rotating pressure field of the compressor stage which moves from right to left in this figure. In order to allow for the traversing of the distortion generator, a tiny gap between the DG and the casing of the inlet duct of about 0.8 mm was necessary. However, this gap was small enough to avoid bias effects.

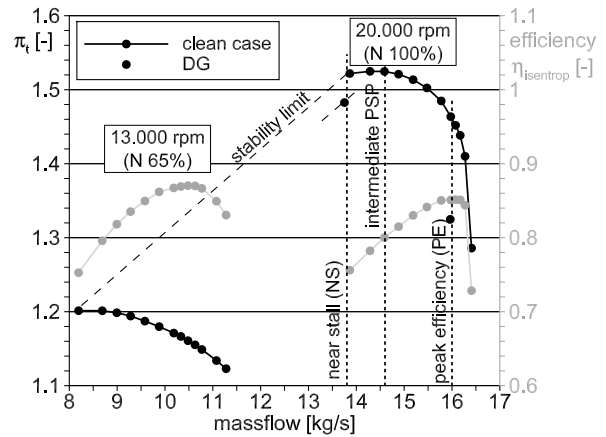


Fig. 3 Characteristics of the compressor stage

Darmstadt Transonic Compressor - DTC	
rotor blades	16
stator vanes	29
rotor diameter	380 mm
hub-to-tip ratio	0.51
design massflow	16 kg/s
design rotor speed ( $N_{100\%}$ )	20.000 rpm
maximum DC power	800 kW
maximum torque	350 Nm

Table 1 Design parameter of the Darmstadt Transonic Compressor (DTC)

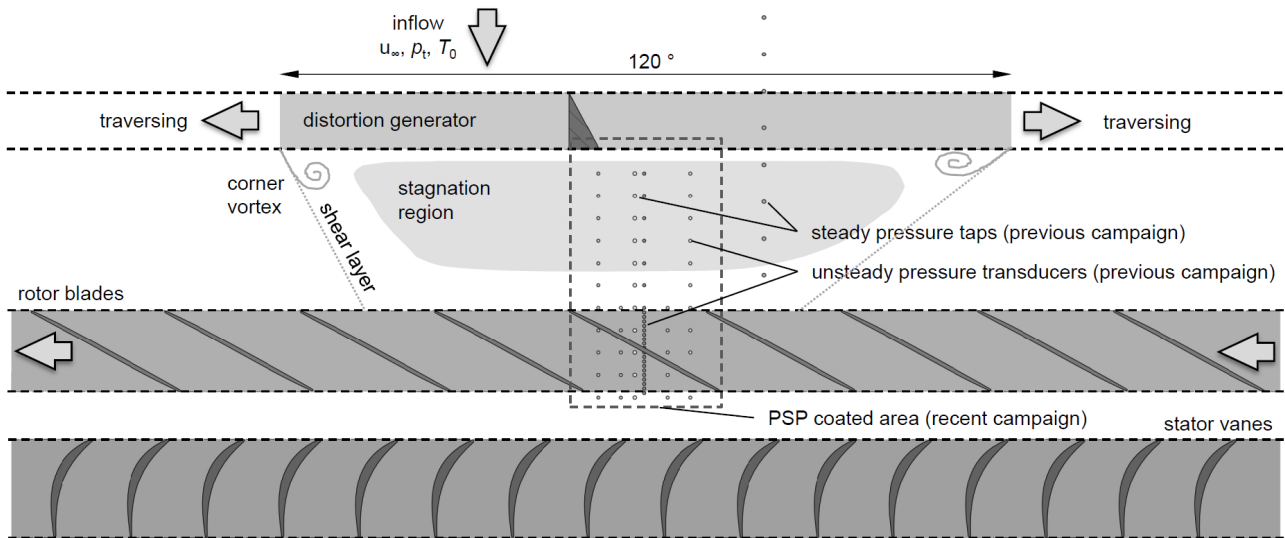


Fig. 4 Flow topology and pressure measurement positions in the wake of the distortion generator upstream of the rotor stage (inflow approaches from the top)

## 4 Experimental Setup and Methodology

### 4.1 PSP Measurement Setup

The DTC's test section case was equipped with a frame covering an arc angle of  $20^\circ$  and extending over 149 mm from the DG until the rear end of the rotor stage, as highlighted by the rectangular dashed box in the center of Figure 4. It allowed the equipment with different measurement instrumentation. For an initial static pressure measurement campaign, this part was equipped with several steady and unsteady pressure sensors (*Kulite XCS-062*) sampled with 500 kHz. The experimental results of this campaign are widely published in [17]. They shall serve as a reference data set for the pressure-sensitive paint measurements presented here.

For the PSP measurements, the frame in the test section was equipped with a transparent window made from Plexiglas (PMMA) which incorporated 2 temperature and 3 static pressure measurement positions. The flow side of the window was coated with dual-luminophore PSP, see left of Figure 5. The paint's absorption peak is at 400 nm. It emits in two wavelength bands; the temperature band  $\lambda = 550 \pm 40$  nm and the pressure band  $\lambda = 660 \pm 50$  nm, according to [5]. The window was marked with circular markers for image registration using a rotating pen mounted in the chuck of a milling machine. Paint excitation was made from the outside of the wind tunnel with two 405 nm high-power LEDs (*Luminus*, USA), each with 10 W optical power, which were operated in pulsed mode with a pulse duration of roughly 1 s. The intensity was recorded using two 11 Mpx CCD cameras (*PCO*, Germany) with appropriate optical band pass filters of high optical density. The

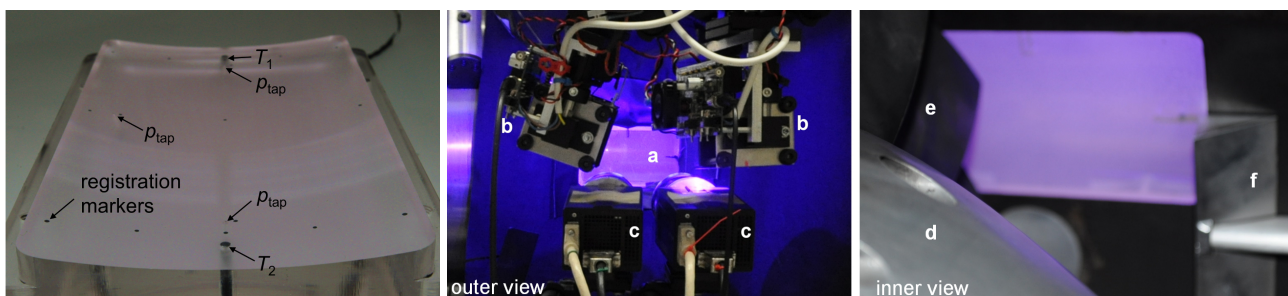


Fig. 5 Experimental setup for the PSP measurements; *left*: PMMA test section window coated with dual-luminophore pressure-sensitive paint and registration markers, equipped with pressure and temperature sensors; *center*: outside view of experimental setup with window (a),  $2 \times 405$  nm high power LEDs (b),  $2 \times 11$  Mpx CCD cameras (c); *right*: test section from the inside with spinner (d), rotor (e) and distortion generator (f).

arrangement of measurement equipment is shown in Figure 5 (*center*). The right of Figure 5 shows a view on the spinner and the rotor downstream of the DG. A static pressure data set was available at two mass flow rates from previous campaigns, as indicated by the isolated symbols in Figure 3.

## 4.2 Methodology

PSP measurements were performed at peak efficiency (PE -  $\dot{m} = 16.1$  kg/s), at near-stall conditions (NS -  $\dot{m} = 13.9$  kg/s) and at an intermediate point (IP -  $\dot{m} = 14.6$  kg/s), as indicated by the dashed vertical lines in Figure 3. The image and sensor data was continuously acquired during an envelope according to Figure 6. The graphs show the temperatures at the DG ( $T_1$ ) and in the center of the rotor disc ( $T_2$ ). As soon as a temperature gradient of  $\Delta T_2 < 0.1$  K was reached, the PSP image acquisition started from the DG's first angular position. It was traversed from  $\varphi = -20 \dots 140^\circ$  with  $\Delta\varphi = 20^\circ$ . A data point was measured on the opposite side of the DG center at  $\varphi = 240^\circ$  which gave an impression of the quasi-undisturbed flow.

Ten dark images for intensity offset correction were acquired. The LEDs flashed continuously at the camera's entire integration time of roughly 1 s during the signal image acquisition. Fifty 'wind-on' samples were recorded at 1 Hz,  $\approx 1$  minute per angular DG position, as indicated by the gray bars in the plots. The 'wind-off' samples at reference conditions were acquired after the wind tunnel shut-down. The pressure from three pressure ports was scanned synchronously with the signal image acquisition. Since all data was time-stamped, the envelope reconstruction could be made in a post-processing procedure. The PMMA window was cleaned from PSP, marked and re-coated after each envelope in order to avoid bias errors due to paint layer contamination and thermally deactivated luminophores. Data evaluation was performed with an in-house Matlab routine, see [1]. The results were projected on a rectangular mesh of the PMMA window which had an axial and lateral spatial resolution of 1 mm. All angular positions were stitched in one data set and in-situ corrected using a global fit function  $p_{PSP,corr} = F(p_{tap}, \varphi)$ . The correlation between raw PSP data and pressure tap data was  $R^2 = 0.86 \dots 0.93$  (lower for NS conditions).

## 5 Results

An overview of the surface pressure topology measured with PSP is given in Figure 7. The plots show the normalized static pressure ratio  $\pi_s = p/p_{t,inlet}$  whereas the missing angular positions (measured:  $200^\circ$  out of  $360^\circ$ ) were added up with data from  $\varphi = 240^\circ$  for presentation purposes. For comparison, the color map is

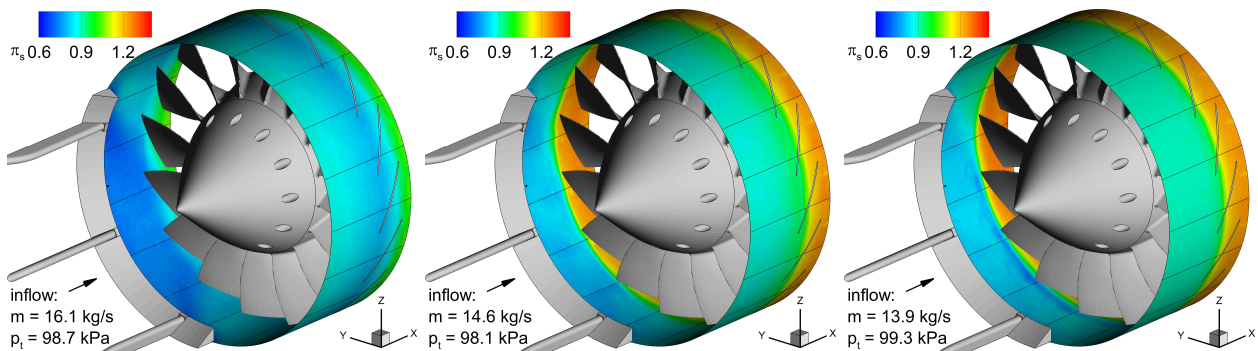


Fig. 7 Topology of the  $\pi_s = p/p_{t,inlet}$  measured with pressure-sensitive paint at three mass flow rates, *left*: PE, *center*: IP and *right*: NS. Missing data was added up with the  $\varphi = 240^\circ$ -measurement case for presentation purposes.

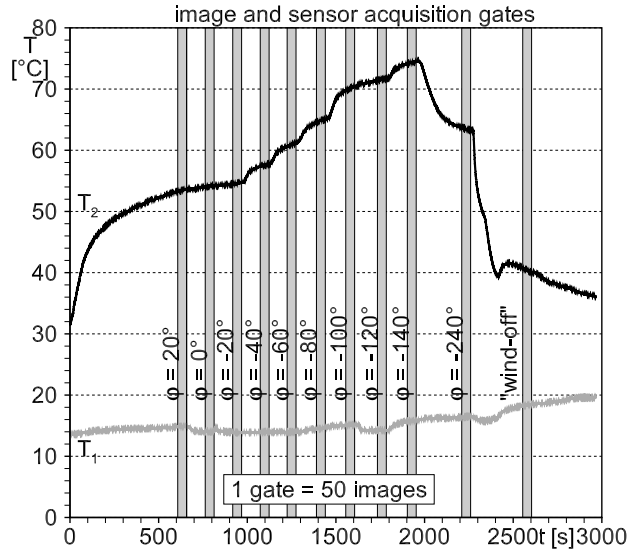


Fig. 6 Image and sensor data extraction from envelope data

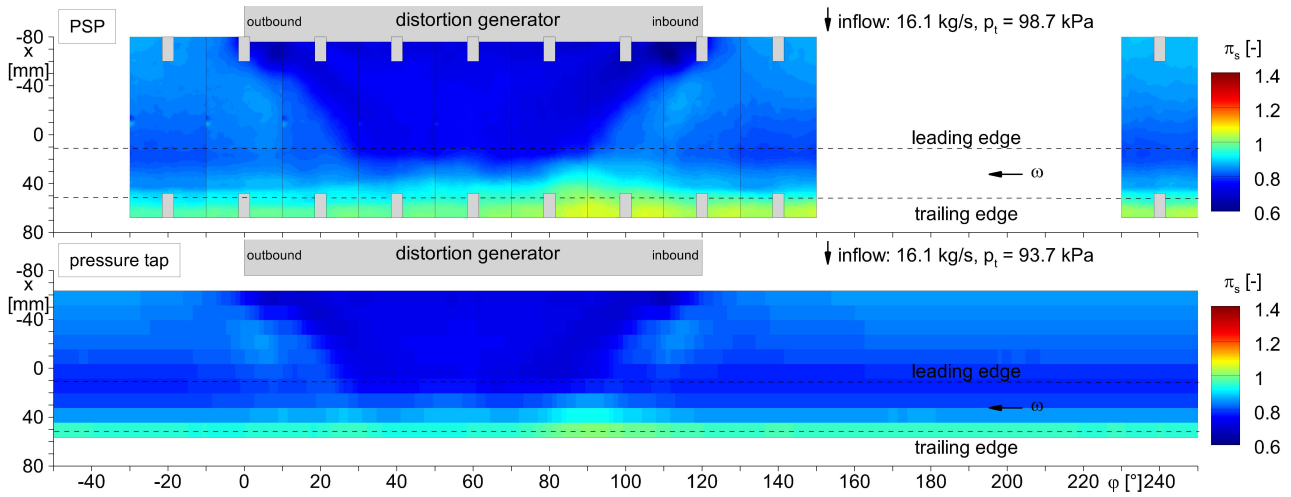


Fig. 8 Comparison of the static pressure ratio  $\pi_s$  from two isolated experimental campaigns measured with PSP (*top*) and a static pressure tap array (*bottom*) for PE ( $\dot{m} = 16.1$  kg/s). Display of data along the angular position  $\varphi$ . The distortion generator was traversed in both campaigns.

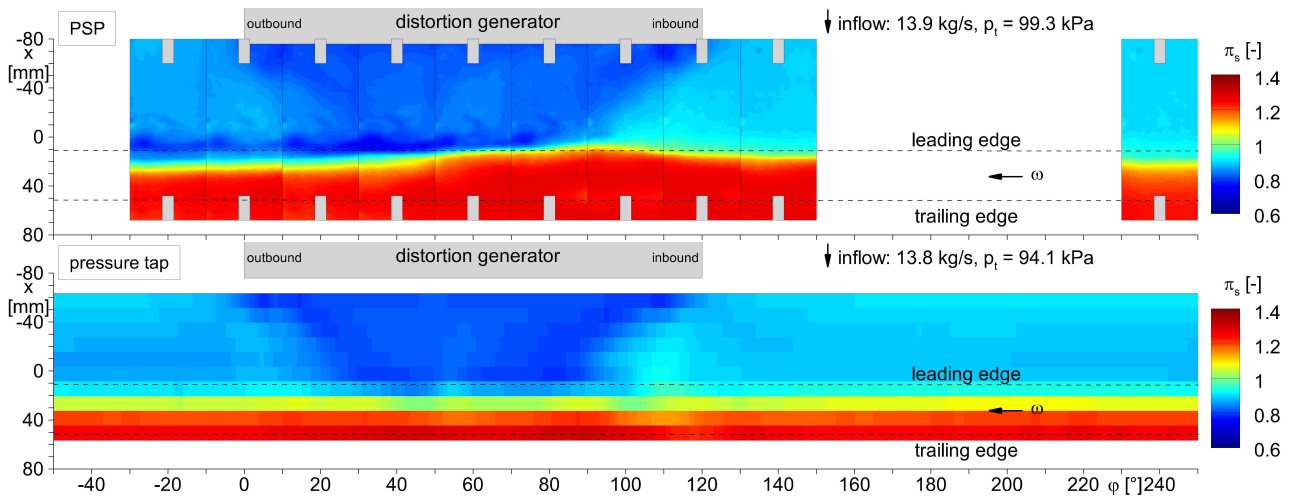


Fig. 9 Comparison of the static pressure ratio  $\pi_s$  from two isolated experimental campaigns measured with PSP (*top*) and a static pressure tap array (*bottom*) for NS ( $\dot{m} = 13.9$  kg/s). Display of data along the angular position  $\varphi$ . The distortion generator was traversed in both campaigns.

identical in all three figures. The flow approaches from negative  $x$  before it is disturbed by the DG. A comparison with the present data from the static pressure measurements was made in Figures 8 for PE and 9 for the NS conditions. The axial coordinate  $x$  is plotted versus the angular position  $\varphi$ . All following data is represented in its actual spatial resolution where the flow approaches from the top. The rotor's tip leading and trailing edges are indicated by the dashed horizontal lines. The rotation direction is from right to left along negative  $\varphi$ . The PSP results in the vicinity of the pressure and temperature sensors were blanked out with tiny gray boxes. A very good qualitative agreement between the corresponding data sets for both conditions is obvious. The strong pressure gradients, especially in the wake of the DG and at the entry of the rotor can be precisely located in the PSP data, whereas the pressure tap resolution is too sparse to do so. A distinct low pressure region is present downstream of the distortion generator. Especially at PE conditions, the agreement between both pressure maps is very good (e.g. at the corners of the DG or at the rotor inlet plane). A quantitative assessment of the mismatch between the results of both campaigns is shown in Figure 10. The local deviation  $1 - \frac{\pi_{s,PSP}}{\pi_{s,tap}}$  [%] is shown color-coded for PE (*top*) and NS (*bottom*). The deviation is obviously stronger in areas which are aerodynamically and thermally highly loaded, as it occurs for the rotor stage. The remaining parts show an agreement within 2%. The main reason for these large local deviations is probably related to the high surface

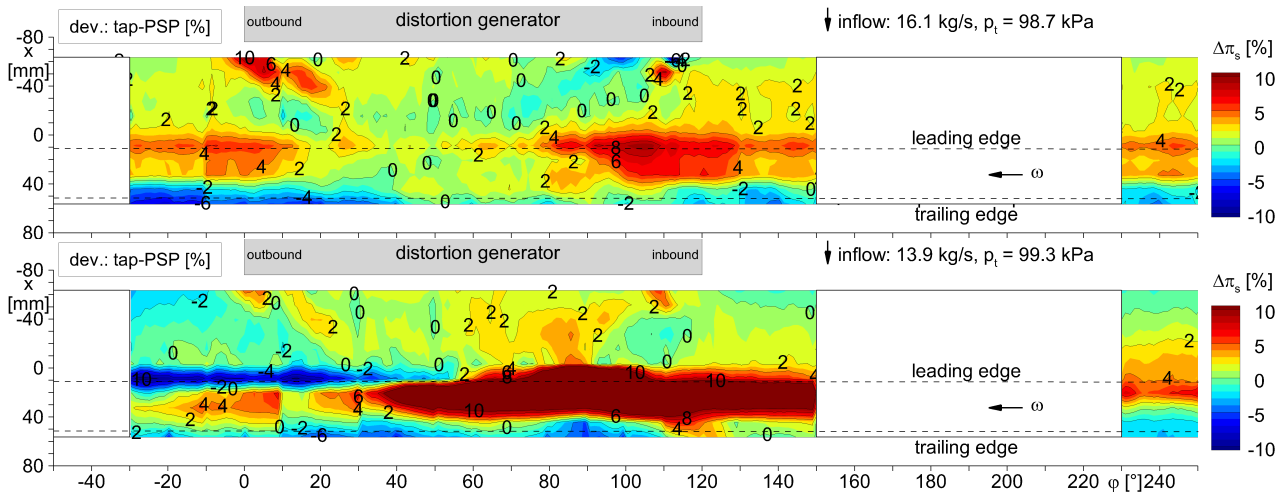


Fig. 10 Spatial deviation  $1 - \frac{\pi_{s,PSP}}{\pi_{s,tap}}$  in percent between PSP and pressure tap data. The spatial resolution is the same as for the pressure tap data but the contour values are flooded for the parallel line display.

temperatures. Continuous contamination of the PSP layer also played a role. Due to high centrifugal forces, dust and soot particles transported with the inlet air were skidded on the wall and led to a continuous signal degradation of the paint. But this effect was expected to be in the same order as the average deviation. The fact which holds this assumption is that the ratio of PSP data at  $\varphi = -20^\circ$  and at  $\varphi = 240^\circ$  showed similar values. Literally speaking, the data acquisition time increased with decreasing angular position  $\varphi$  so the contamination effect should also increase with time. In any event, this plot appears to predict slightly too large areas of high uncertainty due to the coarse axial resolution of the pressure tap data. The PSP data was sampled down to the same data grid.

Figure 11 finally shows the comparison of PSP data extracted at the positions of the pressure taps for each DG angle at PE and NS flow conditions. The RMS of the deviation between PSP and tap data at the tap positions was  $\Delta p_{rms} = 1.3\%$  for PE and  $\Delta p_{rms} = 3.5\%$  for NS.

As mentioned earlier, the dual-luminophore PSP allowed to reduce the paint's temperature effect using a  $T$ -sensitive luminophore. The isolated  $T$ -images were evaluated for Figure 12. It must be noted that the contamination also biased these results by a certain amount. A quantification was not possible since there were only two temperature measurement positions. Due to the continuous temperature rise during the wind tunnel run, the figure presents the temperature gradient  $\Delta T$  for each spatial position with respect to  $T_1$  at PE conditions (top) and for IP (bottom). A temperature gradient of  $\Delta T \leq +60\text{K}$  at some positions, especially for the IP case, is present. The flow which approaches the rotor downstream of the inbound DG (at  $\varphi = 120^\circ$ ) caused a lowered effective incidence as a consequence of the blockage. This led to a stronger compression and a higher static surface temperature. In contrast, at the opposite side downstream of the outbound DG (at  $\varphi = 0^\circ$ ) the incidence is obviously increased which led to a stronger suction peak at the blade's leading edge followed by a lower static temperature as indicated by

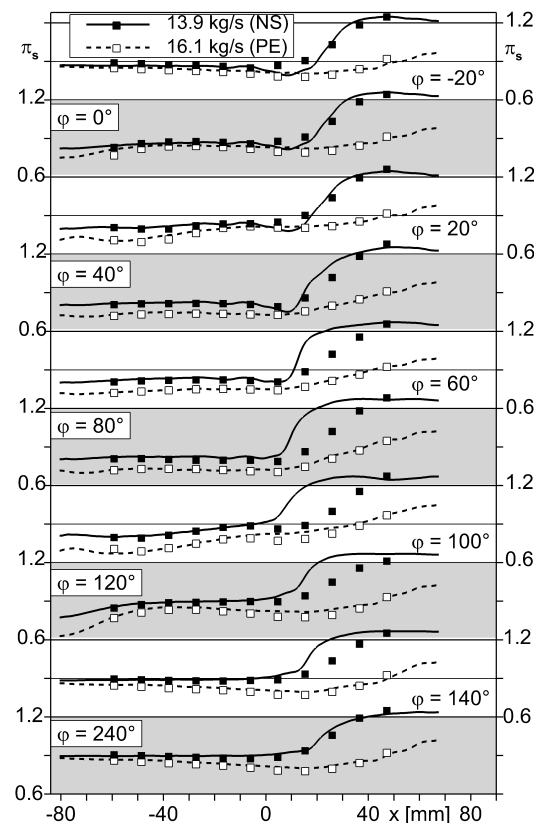


Fig. 11 Comparison of center line data extracted from PSP (solid lines) at the pressure tap positions (symbols) for all angular positions  $\varphi$

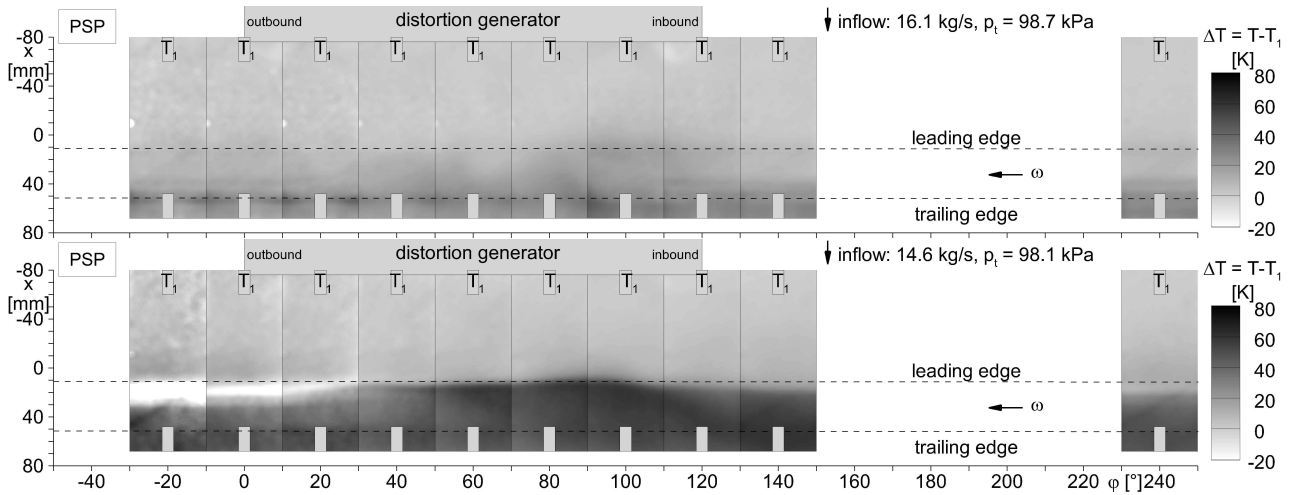


Fig. 12 Comparison of the surface temperature gradient  $\Delta T = T - T_1$  for PE (*top*) and IP (*bottom*) extracted from the temperature-sensitive luminophore in the PSP

the negative temperature gradient. Finally, the wall pressure gradient in the direction of the flow  $dp/dx$  was computed in Figure 13 for all compressor operation points (*top*: PE, *center*: IP, *bottom*: NS). Areas of dark red color indicate a positive pressure gradient of  $dp/dx > 5$  kPa/mm.

At the angular position of the quasi-undisturbed flow ( $\phi = 240^\circ$ ) the compressors behavior to the throttling of the mass flow can be characterized. The positive pressure gradient moves upstream with reduced mass flow rates whereas its strength increases. It must be reflected that the dashed lines in all the figures represent the leading and trailing edges of the tip airfoil. As a consequence of the blade's twist and tapering, the pressure gradient lines can appear to move virtually downstream away from the airfoil, especially at PE conditions. A system of several parallel lines of positive pressure gradient is present for the PE and the IP operation points. It is assumed that these lines represent the time-averaged footprint of the blade's shock system at the wall. A sys-

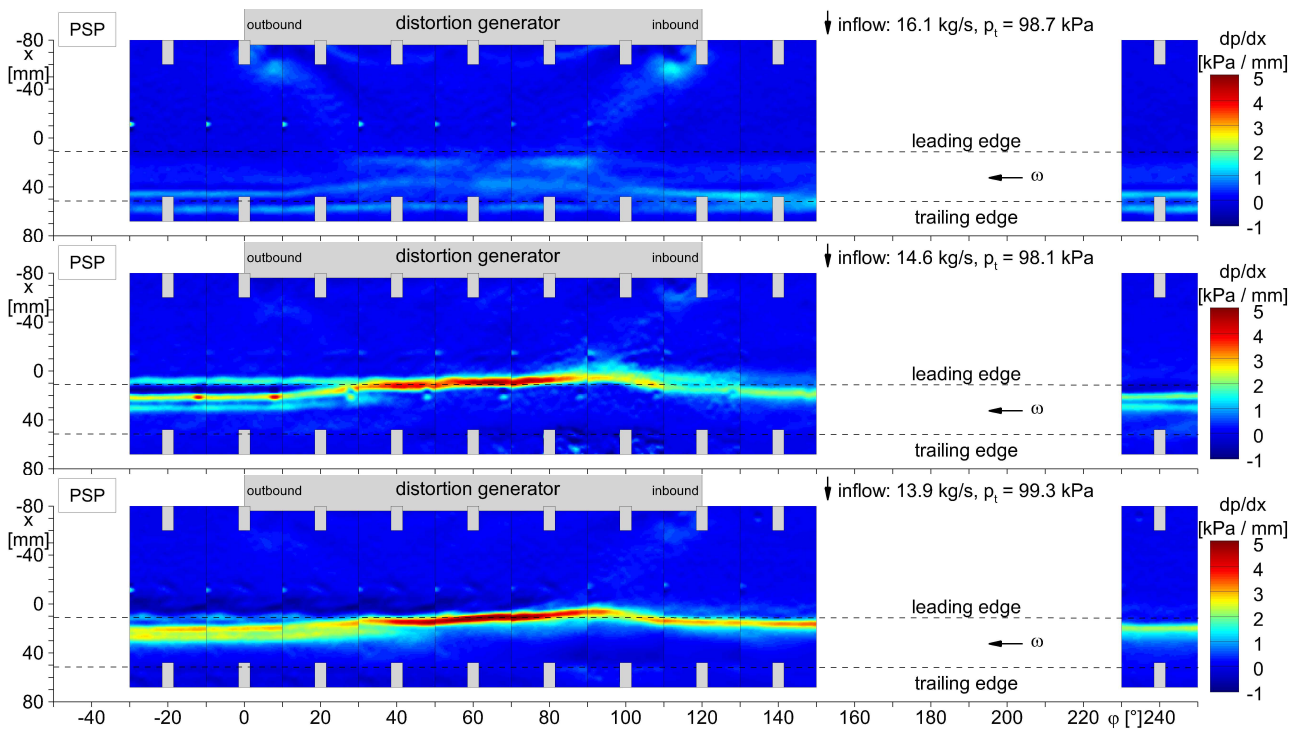


Fig. 13 Comparison of the axial pressure gradient  $dp/dx$  as measured with pressure-sensitive paint for PE conditions (*top*), for the IP (*center*) and for NS conditions (*bottom*)

tem of two shocks typically develops, according to e.g. [14]; one detached separation upstream of the leading edge, where the tip flow reaches supersonic speed; and a second at the critical cross section between the suction and the pressure side of two consecutively passing blades. In any case, a substantial isolated interpretation of the origin of these pressure gradients from the results seemed to be rather complicated without additional information from the flow field. Nevertheless, at aerodynamically highly loaded conditions, i.e. IP and NS, the rotor seems to be more sensitive to the inlet distortions what forced the system of several gradient lines merging into one.

At the remaining angular positions, the compressor's reaction on the distortion generator can be characterized. The central wake of the DG seems to have a throttling effect on the compressor, indicated by the pressure gradient lines, which move further upstream towards the DG and also by a further increase of their strength, compare also [17]. At the inbound DG position, the gradient appears to be very sharp and strong, whereas at the outbound position, it has recovered due to the increased incidence and the gradient lines are shifted back downstream. A third gradient line develops at the outbound DG for IP conditions which is not present in the other operation points. Unfortunately, no reference data set was present for the IP case. For now, it remains unclear if this gradient is physical or if it is an artifact from contamination or temperature.

As already shown in the previous figures, the pressure ratio across the rotor, and hence the pressure gradient, is lowest for PE conditions. The position and the spatial extent of the corner vortices at the DG's in- and outbound ends can be characterized from these plots as well. The vortex footprint is the strongest for the PE case because the shear forces at the edges of the DG are expected to be the strongest for the highest mass flow rates.

## 6 Conclusions

The wall pressure distribution across the Darmstadt Transonic Compressor disk with disturbed inflow from a distortion generator was successfully characterized by means of the pressure-sensitive paint measurement technique at various operating points ranging from peak efficiency to near-stall conditions. The presented results are both, quantitatively and in terms of the flow topology, in very good agreement with steady static pressure tap data. The deviation in the compared results from both experimental campaigns was between 1.3 % and 3.5 %, lower at peak efficiency. Due to the high spatial resolution of the PSP measurements, the results yield much more physical information than the classical probe data. In particular, the behavior of the compressor at throttling mass flow rates and its steady-state reaction to massive inlet distortions were resolved in detail.

The reference pressure data set was measured in roughly 5 hours at 11 axial pressure taps for 290 circumferential positions. The spatial resolution of the PSP results in axial direction was roughly 14 times higher (it could be any arbitrary grid resolution), but it was measured in only one fifth of the tap acquisition time. It was the first time that the wall pressure topology across the rotor disc of the DTC could be resolved with such high spatial resolution. This resolution enabled the identification of further flow details, such as very sharp pressure gradients, especially across the rotor disk, which could not be resolved with the pressure tap array. The results showed the position and strength of the pressure gradient across the rotor moving upstream while the compressor is throttled. The influence of the DG to the rotor was comparable to a further reduction of the mass flow rate, which was clearly shown in the PSP results. This 120° distortion generator effectively produced a massive inlet distortion over  $\approx 80^\circ$  in its central wake leading to a strong, but locally very distinct, forming of the pressure gradient.

The accuracy of the results showed a good performance of the dual-luminophore pressure-sensitive paint even in conditions with strong surface temperatures or minor paint layer contamination. The PSP measurement uncertainty, especially for PE conditions, was comparable to conventional transonic PSP measurements under typical temperature and pressure conditions, compare [1]. The benefit of increased spatial resolution at saved measurement time exposed the potential of the PSP measurement technique for the characterization of compressor flows. A detailed comparison of these results with available numerical simulations can generate a valuable data base for the future design of jet engine compressors and may lead to the reduction of safety margins with respect to massive unsteady inlet distortions.

## Acknowledgment

The partial funding of this paper within the FP7 framework's project NIOPLEX and the collaboration within the FOR-1066 research unit of DFG - Deutsche Forschungsgemeinschaft is acknowledged by the authors.

## References

- [1] Bitter M (2014): Characterization of a turbulent separating/reattaching flow using optical pressure and velocity measurements. Dissertation, Bundeswehr University Munich, Shaker-Verlag Aachen, ISBN: 978-3-8440-2539-2.
- [2] Engler RH, Klein C, Trinks O, Zielinski M, Hennecke DK, Kablitz S (2000): Pressure sensitive paint measurements at a transonic compressor stage. In: Measurement Techniques in Transonic Flow, Symposium, Florence, Italy.
- [3] Gregory JW, Sakaue H, Liu T, Sullivan JP (2014): Fast Pressure-Sensitive Paint for Flow and Acoustic Diagnostics. *Annual Review of Fluid Mechanics*, Vol. 46, pp. 303-330, DOI: 10.1146/annurev-fluid-010313-141304.
- [4] Hayami H, Hojo M, Matsumoto M, Aramaki A, Yamada K (2002): Application of pressure sensitive paint measurement to a low-solidity cascade diffuser of a transonic centrifugal compressor. *Journal of Visualization*, Vol. 5, pp. 45-50, DOI: 10.1007/BF03182602.
- [5] Innovative Scientific Solutions Incorporated (2015): <http://psp-tsp.com/>.
- [6] Lieser JA, Biela C, Pixberg CT, Schiffer H-P, Schulze S, Lesser A, Kähler CJ, Niehuis R (2011): Compressor Rig Test with Distorted Inflow using Distortion Generators. In: 60. Deutscher Luft- und Raumfahrtkongress, Bremen, Germany.
- [7] Liu T, Sullivan JP (2005): Pressure and Temperature Sensitive Paints. Vol. 1, Springer-Verlag, Berlin, Heidelberg, New York, ISBN: 978-3-540-22241-5.
- [8] Khalil GE, Costin C, Crafton J, Jones G, Grenoble S, Gouterman M, Callis J B, Dalton LR (2004): Dual-luminophore pressure-sensitive paint: I. Ratio of reference to sensor giving a small temperature dependency, *Sensors and Actuators B: Chemical*, Vol. 97, pp. 13-21, DOI: 10.1016/S0925-4005(03)00484-2.
- [9] Navarra KR, Rabe DC, Fonov SD, Goss LP, Hah C (2001): The application of pressure- and temperature-sensitive paints to an advanced compressor. *Journal of Turbomachinery*, Vol. 123, pp. 823-829, DOI: 10.1115/1.1400116.
- [10] Niehuis R, Lesser A, Probst A, Radespiel R, Schulze S, Kähler CJ, Spiering F, Kroll N, Wartzek F, Schiffer HP (2013): Simulation of Nacelle Stall and Engine Response. 21st ISABE Conference, September 9-13, ISABE-2013-10135.
- [11] Radespiel R, Francois D, Hoppmann D, Klein S, Scholz P, Wawrzinek K, Lutz T, Auerswald T, Bange J, Knigge C, Raasch S, Kelleners P, Heinrich R, Reuß S, Probst A, Knopp T (2013): Simulation of Wing Stall. 43rd AIAA Fluid Dynamics Conference, June 24-27, 2013-3175.
- [12] Radespiel R, Heinze W (2014): SFB 880 - fundamentals of high lift for future commercial aircraft. *CEAS Aeronautical Journal*, Vol. 5, pp. 239-251. DOI: 10.1007/s13272-014-0103-6.
- [13] Übelacker S, Hain R, Kähler CJ (2014): Flow Investigations in a Stalling Nacelle Inlet Under Disturbed Inflow. In: Proceeding of the 4th International Symposium 'Simulation of Wing and Nacelle Stall', Springer-Verlag, Berlin Heidelberg.
- [14] Saravanamuttoo HIH, Roger GFC, Cohen H, Straznicki PV (2008): Gas Turbine Theory. 6th ed., Pearson Education Ltd. Essex, ISBN: 978-0132224376.
- [15] Schulze G, Blaha C, Hennecke DK, Henne JM (1995): The performance of a new axial single stage transonic compressor. In: International Symposium on Air Breathing Engines.
- [16] Suryanarayanan A, Mhetras SP, Schobeiri MT, Han JC (2009): Film-cooling effectiveness on a rotating blade platform. *Journal of Turbomachinery*, Vol. 131, DOI:dx.doi.org/10.1115/1.2752184.
- [17] Wartzek F, Brandstetter C, Holzinger F, Schiffer H-P (2015): Response of a Transonic Compressor to a Massive Inlet Distortion. In: 11th European Conference on Turbomachinery Fluid Dynamics and Thermodynamics, Madrid, Spain.